Plasmonic Cu nanoparticle on reduced graphene oxide nanosheet support: An efficient photocatalyst for improvement of near-infrared photocatalytic H₂ evolution

Piyong Zhang, Ting Song, Tingting Wang, Heping Zeng[*]

Key Laboratory of Functional Molecular Engineering of Guangdong Province, School of Chemistry and Chemical Engineering, South China University of Technology, Guangzhou, 510641, PR China

ARTICLE INFO

ABSTRACT

Cu nanoparticles (NPs) are low-cost plasmonic metals and have been used for photocatalytic hydrogen evolution due to their surface plasmon resonance (SPR) effect. An efficient photocatalyst consisting of plasmonic Cu NPs on reduced graphene oxide (rGO) nanosheets support (Cu/rGO) is successfully prepared by a facile *in-situ* photoreduction process to form multiple nanoscale junctions for enhancement of photocatalytic hydrogen evolution. Compared to individual Cu NPs, the coupling to rGO nanosheets produces a higher photocatalytic ability with the highest H_2 evolution rate of 59 mmol $g^{-1} h^{-1}$ for sample **C**, which contains 1.0 wt% of rGO nanosheets. The rGO nanosheet possesses an extremely high conductivity and, can accept and transfer photo-generated electrons with no barrier. Therefore, recombination of photoinduced charges can be efficiently suppressed and the accepted electrons can be rapidly transferred to reactive sites for H_2 evolution across its two-dimensional plane. More importantly, a near-infrared photocatalytic activity for sample **C** was obtained under monochromatic light irradiation at 800 and 900 nm due to the broad spectrum response of plasmonic Cu NPs. Furthermore, a possible reaction mechanism is proposed for the photocatalytic activity improvement as well as the detailed charge transfer condition.

1. Introduction

H_2 evolution is an economical approach for the conversion of solar energy into chemical fuels because H_2 possesses a high energy density, is a useful by-product of water from combustion, and produces zero carbon emission [1]. Plasmonic metal nanoparticles (Cu, Ag, Au, etc.) have attracted much attention for H_2 evolution through the surface plasmon resonance (SPR) effect [2–8]. The SPR effect is the resonant collective oscillation of electrons in plasmonic metal nanoparticles (NPs) that occurs, when the frequency of incident light matches the frequency of electrons oscillating against the restoring force of positive nuclei [9–11]. Photocatalytic H_2 evolution by Cu NPs has been reported due to their strong SPR effect in a broad spectral range, promising photocatalytic activity, high conductivity and low cost [12–15]. Chemical stability of Cu NPs is the primary challenge for their use in photocatalytic H_2 evolution. Therefore, a facile process to obtain Cu NPs with high stability for H_2 evolution should be considered.

Graphene is a two-dimensional network of sp^2-bonded carbon atoms that, has attracted great research interest due to its special properties such as excellent optical transmittance, large theoretical specific surface area, exceptional conductivity and fast room-temperature mobility of charge carriers [16–22]. Graphene can accept photogenerated electrons with no barrier due to its high work function and the accepted electrons can rapidly migrate across its two-dimensional plane because of its high conductivity, which can promote reactivity on adjacent materials [23]. This outstanding electron-hole separation property suggests that the photocatalytic system with an ideal component of graphene should be considered. Graphene-based photocatalytic materials such as, TiO_2/graphene [24], Cu_2O/graphene [25], and BiOCl/graphene [26], have been extensively investigated. However, to the best of our knowledge, no investigation of Cu nanoparticle on reduced graphene oxide (rGO) nanosheet support has been reported for photocatalytic H_2 evolution. Independent control and rational design of the Cu/rGO system result in an environmentally benign and earth-abundant photocatalyst for H_2 evolution.

Based on our research [12–14,27–29], our group reported a convenient *in-situ* process for the preparation of Cu NPs on rGO nanosheet support under vacuum conditions. Photocatalytic H_2 evolution of Cu NPs and Cu/rGO composite was investigated under solar and near-infrared light irradiation using lactic acid solution as a sacrificial agent,

and a higher H_2 evolution rate for Cu/rGO was achieved than using Cu NPs alone. Both Cu NPs and Cu/rGO show obvious photocatalytic ability under monochromatic light irradiation at wavelengths of 800 and 900 nm. In addition, the chemical stability of the photocatalyst was also studied by the cycling test and structural characterizations.

2. Experimental

2.1. Materials

$NaNO_3$ (AR), graphite powder, H_2O_2 (35 wt%), concentrated H_2SO_4 (18 M), $KMnO_4$ (AR), lactic acid (97%), Triton X-100 and copper acetate hydrate ($Cu(CH_3COO)_2 \cdot H_2O$ AR) were purchased from Aladdin. Deionized water was used in all experiments, and the reagents were used directly without further treatments.

2.2. Synthesis of graphene oxide (GO) nanosheets

GO nanosheets were prepared using natural graphite powder via a modified Hummer's method [30]. Firstly, 1.25 g of $NaNO_3$ and 2.5 g of graphite powder were dispersed in a solution of concentrated H_2SO_4 (60 mL) under ice bath conditions. The temperature of the mixture remained at 0 °C, followed by gradual addition of 7.5 g of $KMnO_4$. The mixture was then stirred at 30 °C for 6 h to allow oxidation. Subsequently, the mixture was diluted with 230 mL of deionized water and stirred at 90 °C for 20 min. The reaction was concluded by adding 6 mL of H_2O_2 to reduce the residual $KMnO_4$, and the mixture with a brilliant yellow color was obtained after the reduction reaction. The mixture was washed there times with deionized water, and then solid GO nanosheets were isolated by freeze-drying.

2.3. Characterization

X-ray diffraction (XRD) patterns were collected by a D8 X-ray diffractometer (German, Bruker AXS) with Cu-Kα radiation (λ = 1.54178 Å). X-ray photoelectron spectroscopy (XPS) data were recorded on a Kratos Axis-Ultra DLD (equipped with AES) instrument, using a monochromatized Al-Kα as the excitation source (150 W). Transmission electron microscopy (TEM) and high-resolution transmission electron microscopy (HRTEM) images were obtained using a JEOL JEM-2100 electron microscope. The general morphologies of the samples were investigated by scanning electron microscopy (SEM, Zeiss Merlin, Germany, Zeiss Co.) UV–vis diffuse reflectance data were obtained in the spectral region of 200–900 nm with a U3010 (Hitachi, Japan, referenced by $BaSO_4$) spectrophotometer. Photo-luminescence (PL) measurements at room temperature were collected on a Hitachi F-4500 fluorescence spectrophotometer with a 450 W xenon lamp as the excitation source. Raman spectra were recorded using a Laser Confocal Raman Microscopy system (LabRAM Aramis, H.J.Y, France). Fourier transform infrared (FT-IR) spectra were collected using a Nicolet 670 spectrometer.

2.4. Photocatalytic hydrogen evolution

Photocatalytic hydrogen evolution was performed at approximately 25 °C in a gas-enclosed side irradiation system. Cu/rGO nanocomposite was synthesized by an *in-situ* photoreduction method [12,31]. GO, Triton X-100, lactic acid and copper acetate solution were suspended in deionized water in a 300 mL Pyrex reaction cell with side irradiation from a 300 W Xenon lamp (PLS-SXE300CUV, Perfect light. Co. Ltd., Beijing). The mixture solution was completely degassed for about 30 min, followed by irradiation with the xenon lamp. The sample components are shown in Table S1, and a schematic of the synthesis and photocatalytic reaction process for the sample is displayed in Scheme 1. After irradiation, GO nanosheets were reduced to rGO nanosheets and Cu NPs were generated on the surface of rGO nanosheets

at the same time. Meanwhile, photocatalytic H_2 evolution was carried out. The rGO content is 0.1 wt%, 0.5 wt%, 1 wt%, 2 wt% and 5 wt% (theoretical rGO content) for samples **A**, **B**, **C**, **D** and **E**, respectively. The level of H_2 evolution was determined using online gas chromatography (GC-7900, TCD, N_2 carrier, 5 Å molecular sieve column, Tian mei).

Cu NPs alone and sample **C** were selected to carry out near-infrared photocatalytic H_2 evolution experiments, using monochromatic light irradiation with 800 ± 10 and 900 ± 10 nm bandwidth of band pass filters. Other photocatalytic reaction parameters were unchanged. For characterization, the samples were harvested by centrifugation at 10,000 rpm for 25 min after photocatalytic reaction under nitrogen protection.

A physical mixture of Cu NPs and rGO nanosheets was also investigated for photocatalytic hydrogen evolution. First, 58 mL of deionized water, 10 mL of lactic acid and 1 mL of 2 mmol L^{-1} copper acetate solutions were added in a 300 mL Pyrex reaction cell. Next, the mixture solution was completely degassed for about 30 min, followed by irradiation with a xenon lamp. The H_2 evolution rate was determined using online gas chromatography every hour, and the entire experimental required approximately 5 h. After 5 h of irradiation, 1.2 mL of 0.01 g L^{-1} GO solution and 1 mL of Triton X-100 were added to the above solution, followed by another cycle of degassing and irradiation again. The H_2 evolution rate was also determined by online gas chromatography every hour. Cu NPs were first produced and rGO nanosheets were introduced after 5 h with photoreduction of GO. With the exception of the different order of introduction, the composition of the above solution is identical to that of sample **C**. A physical mixture of Cu NPs and rGO nanosheets was obtained in the solution. In addition, the methods to synthesize Ag, Au and Bi plasmonic materials are described in the supporting information.

2.5. Photoelectrochemical measurements

Photoelectrochemical measurements were carried out using a CHI660C Instruments electrochemical workstation operated in a standard three-electrode configuration with an FTO electrode deposited with sample as the photocathode, a saturated Ag/AgCl electrode as the reference electrode, and a platinum wire as the counter electrode. A 0.1 M Na_2SO_4 aqueous solution (30 mL, pH = 7) purged with N_2 was used as the electrolyte without additive. The working electrode for electrochemical analysis was prepared by drop-casting sample/water suspensions onto the as-washed FTO glass to form the film electrode, and was then allowed to dry at 323 K for 3 h under vacuum conditions. A 300 W Xenon lamp was applied as the simulated sunlight source for the photocurrent measurement.

3. Results and discussion

3.1. Formation and characterization

The morphology and microstructure of sample **C** were analyzed using the SEM, TEM and HRTEM images. Small particles with uniform distribution were observed by SEM images (Fig. 1a) corresponding to Cu NPs, that had a particle size of 11 ± 1 nm (mean size ± standard deviation) based on the wide-range SEM image analysis. Further magnification of the image as shown in Fig. 1b reveals that Cu NPs are successfully loaded on the wrinkled rGO nanosheets surface, implying that the photoreduction approach is effective for the formation of Cu/rGO nanocomposites. The EDX analysis in Fig. 1c exhibits that the composite consists of Cu, C and O. The corresponding elemental mappings (Fig. 1d) are consistent with the EDX spectrum. Note that elemental mappings of C and O show points signifying the presence of C and O throughout these two images due to the existence of rGO nanosheets and conducting resins with high C and O contents; it can also be observed that, the Cu distribution in elemental mapping matches the selected region to some degree. Further observation by TEM imaging
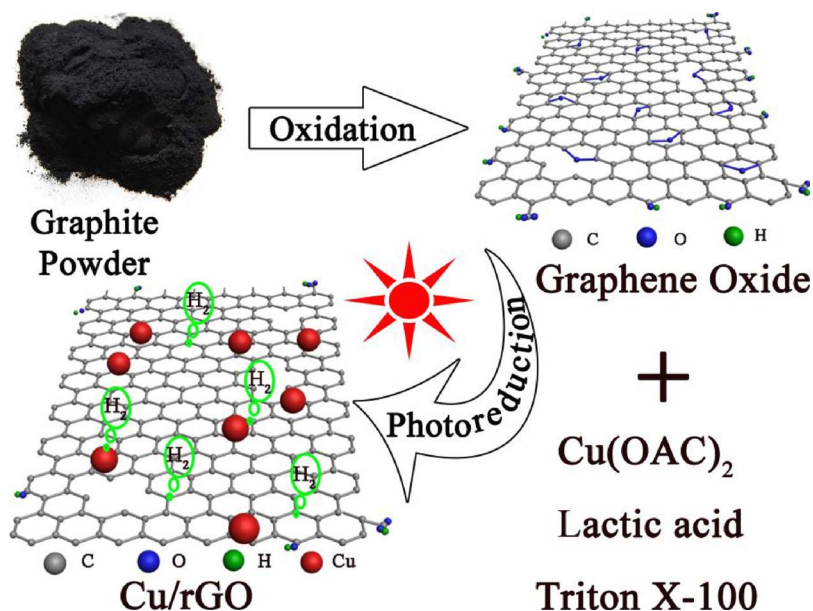
Scheme 1. Illustration of the synthesis and photocatalytic reaction procedure for Cu/rGO.

(Fig. 1e) shows a pronounced nanosheet structure of rGO on the edge of the sample and dark spots that are attributed to Cu NPs. Typical rGO nanosheet structure [16] and Cu NPs (marked by the red circle) are shown in a high-resolution TEM image (Fig. 1f) for further illustration of the formation of Cu/rGO. The lattice spacing of 0.21 nm corresponds to the (111) plane of metallic Cu [12], in which intimate contact with the rGO, providing persuasive evidence for the formation of heterostructures. The photoinduced electrons can smoothly migrate in the heterogeneous interface, obtaining the desired efficient separation of electrons and holes. Examination of the selected area electron diffraction (SAED) pattern presented in Fig. 1g depicts the pattern of Cu with diffraction rings corresponding to the (111) and (200) reflections. In addition, a weak and typical sixfold symmetry is presented in the SAED pattern due to the carbon atoms order in regular benzene hexagons of rGO [32].

In the X-ray diffraction (XRD) pattern of the GO (Fig. 2a), the peak at 9.8° arises from the (002) interlayer spacing [33]. The XRD pattern of the bulk Cu can be perfectly indexed as the face centered cubic copper (JCPDS No. 04-0836) [12], and the peak is very sharp. However, these patterns of samples **A**, **B**, **C**, **D**, and **E** have relatively broad diffraction
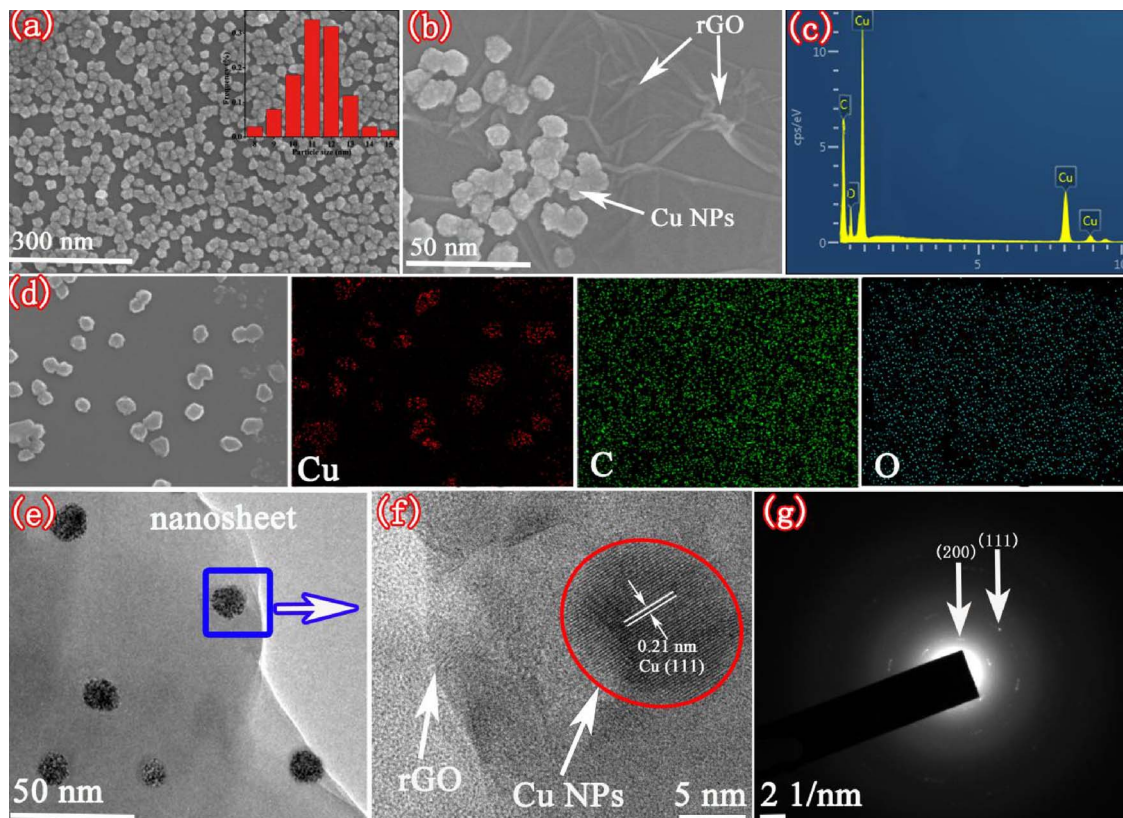
Fig. 1. Morphology of sample **C**: (a) SEM image and size distribution (inset), (b) SEM image, (c) EDX spectrum, (d) elemental mapping patterns, (e) TEM image, (f) HRTEM image and (g) SAED analyses.
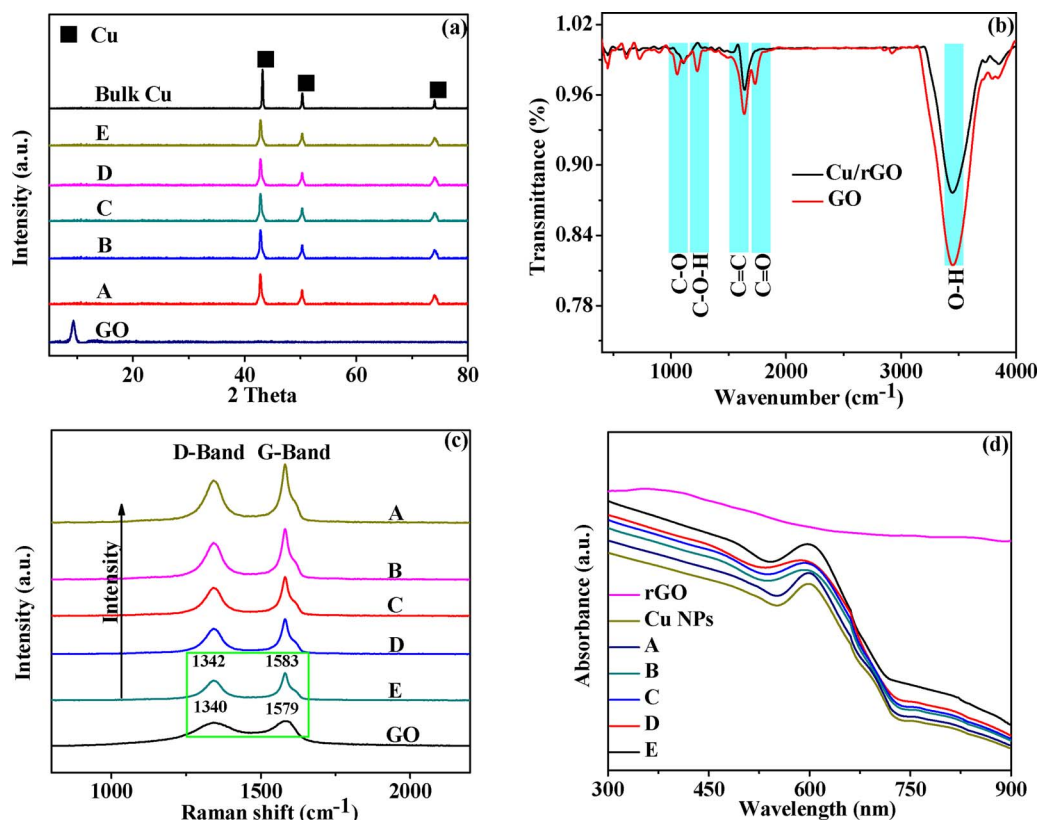
Fig. 2. (a) XRD patterns, (b) FTIR spectra, (c) Raman spectra, (d) UV–vis diffuse reflectance spectra of samples.

peaks compared with bulk Cu due to their nanoscale size [34], suggesting that the Cu particles generated from the photoreduction procedure are nanoscale, as has been demonstrated by the SEM and HRTEM images. The representative peak of GO at 9.8° has disappeared in the XRD patterns of samples **A**, **B**, **C**, **D**, and **E**, indicating that GO was successfully reduced by the photoreduction procedure [35,36]. Samples with high purity were obtained, and no peaks for CuO or Cu_2O were detected in XRD patterns. The addition of GO has a negligible effect on the crystalline formation of Cu, and the face centered cubic copper structure remains unchanged.

Fourier transform infrared (FTIR) spectra of GO and sample **C** (Cu/rGO) were obtained to study different chemical bonds and functional groups (Fig. 2b). For GO, absorbance peaks at 3442, 1730, 1640, 1370 and 1032 cm^{-1} can be related to O−H stretching, C=O stretching of COOH groups, C=C stretching, C−O−H groups stretching and C−O−C stretching vibrations, respectively [37–39]. After the photoreduction process, almost all of these absorbance peaks of the O-containing stretching vibration functional groups in the spectrum of sample **C** either strongly decreased or disappeared entirely. C=O, C−O−H and C−O−C may be completely reduced to C. O−H stretching at 3442 cm^{-1} still exhibits evident absorbance peaks, which should be ascribed to H_2O [40]. No absorbance peaks for Cu NPs can be detected due to their lack of response in infrared spectroscopy. These results imply that GO is successfully reduced by the photoreduction process.

Raman spectra of GO and Cu/rGO samples are presented in Fig. 2c. Among the Raman bands of GO, two specific bands, namely the G (1579 cm^{-1}) and D (1340 cm^{-1}) bands, originated from the in-plane vibration of ordered sp^2-bonded carbon atoms in aromatic conjugated and the out-plane vibration of sp^3 carbons present in the form of defects, respectively [41]. The intensity ratio of the D to G bands (I_D/I_G) for GO was about 1.13, suggesting that epoxide and other oxygen bearing group defects were present in GO [42]. For sample **E**, the positions of the D and G bands were slightly red-shifted to 1342 and 1583 cm^{-1} due to surface strain after loading with Cu NPs [43], and the I_D/I_G ratio increased to 1.51, demonstrating a decrease in the sp^2

domain size [41]. Consequently, new extended sp^2 domains are efficiently formed during the photoreduction process and GO was successfully reduced to rGO. Other Cu/rGO samples show similar phenomena. Moreover, stepwise enhanced intensity of the D- and G-bands for Cu/rGO is observed due to the Surface-enhanced Raman Scattering (SERS) effect of Cu NPs, demonstrating that charge transfer between the rGO nanosheets and Cu NPs occurs under light excitation conditions [44].

Fig. 2d shows the optical absorption spectra of Cu NPs, rGO and Cu/rGO. A typical absorption peak at approximately 600 nm is observed for the solitary Cu NPs due to the SPR effect [12]. Furthermore, an absorbance tail extending to the near-infrared region is observed for Cu NPs, showing potential for the near-infrared photocatalytic reaction. rGO nanosheets exhibit a representative absorption behavior over the entire investigated range of wavelengths [45]. For Cu/rGO nanocomposites, a pronounced enhancement in light absorption intensity is achieved when rGO nanosheets were progressively increased, indicating that the modification with rGO nanosheets can improve the light absorption ability due to the formation of a nanojunction between the Cu NPs and rGO nanosheets [45]. These results suggest that Cu NPs were successfully loaded on rGO nanosheets, and more light consisting of UV–vis and near-infrared photons was absorbed and thus improving catalytic activity.

Fig. 3 displays detailed XPS spectra for sample **C**. The general XPS survey of sample **C** demonstrated that the main constituents are copper, carbon and oxygen (Fig. 3a). The high resolution XPS spectrum of C1 s can be fitted into four peaks as shown in Fig. 3b, which ranging from 281 to 292 eV. The peaks at 284.5, 285.2, 286.0 and 288.4 eV are assigned to the C=C, C−O, C=O and O=C−O configurations, respectively [46]. The O=C−O and C=O bonds are ascribed to the carboxylic and ketone functional groups in the rGO periphery [16,46]. The C−O bond is attributed to the tertiary alcohol and epoxy functional groups on the basal plane of rGO [46,47]. Compared to the C1s spectrum of GO shown in Fig. S1, the amount of O-functional groups greatly diminished after photoreduction treatment, implying that the number of oxygenate
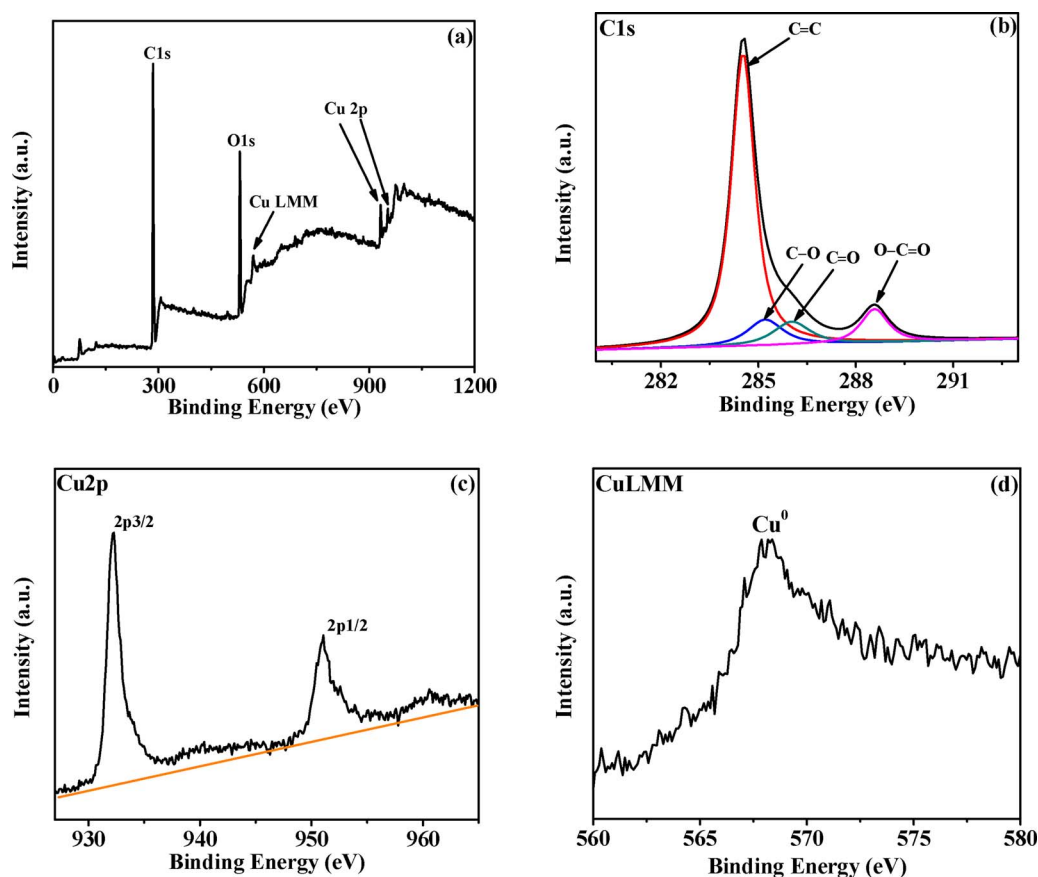
Fig. 3. XPS spectra of sample **C**: (a) full-range XPS spectrum of sample **C**, (b) C1 s spectrum, (c) Cu2p spectrum, and (d) CuLMM spectrum. The C1 s spectrum was decomposed into four peaks fitted using Gaussian functions.

groups was decreased sharply, which is beneficial for the charge transfer between the rGO nanosheets and Cu NPs. The Cu2p spectrum exhibits Cu2p1/2 and Cu2p3/2 spin-orbital splitting of photoelectrons, located at the binding energies of 932.2 and 952.1 eV, respectively [12]. The Cu2p spectrum is ascribed to Cu^0 or Cu_2O due to the lack of a satellite peak located at approximately 943 eV, showing that the high valence state Cu^{2+} species are effectively reduced [13,14]. CuLMM XAES is usually used to distinguish these two states because Cu^0 and Cu_2O have almost the same binding energy of Cu2p1/2 and Cu2p3/2 [13,48]. As shown in Fig. 3d, the peak at 568.3 eV is attributed to Cu^0 [12–14], suggesting that Cu NPs are successfully prepared by the photoreduction approach, which is consistent with the HRTEM and XRD results.

3.2. Photocatalytic hydrogen evolution

H_2 evolution was carried out for the samples in a water/lactic acid mixture solution under solar and near-infrared light irradiation. Lactic acid acts as a hole-scavenger. Lactic acid or rGO nanosheets alone showed no photocatalytic activity toward hydrogen evolution, indicating that hydrogen is generated from *in-situ* Cu NPs through a photocatalytic reaction. As shown in Fig. 4a, a relatively low H_2 evolution rate (28 mmol g^{-1} h^{-1}) is observed for Cu NPs, and other samples combined with rGO nanosheets all showed higher H_2 evolution than Cu NPs alone. The improvement in the photocatalytic ability was solely attributed to the electron acceptor and transporter role played by the rGO nanosheets in the samples. With increasing the content of rGO nanosheets, the H_2 evolution rate of Cu/rGO increased to the highest value at 1 wt% of rGO nanosheets for sample **C**, and is twice as high as that of single Cu NPs. The H_2 evolution rate decreases when the rGO nanosheet content is increased further because excess rGO nanosheets act as the electron-hole recombination centers in the composite, reducing the photocatalytic ability [16,49]. Therefore, suitable level of rGO

nanosheets can enhance the photocatalytic reaction ability due to the optimum electron-hole pair separation.

Operational lifetime is an important property for a photocatalyst. The hydrogen evolution experiment of sample **C** was monitored for five consecutive runs under the same conditions. A slight activity decrease is observed upon repeated use (Fig. 4b), demonstrating the remarkable stability of the catalyst. The X-ray diffraction results of sample **C** (Fig. S2) used for 5 rounds show no obvious change for Cu NPs. The XPS spectra of sample **C** before and after the recycle test also do not show observable changes for Cu2p and CuLMM (Fig. S3). Furthermore, surface element compositions (Table S2) were also determined by XPS, and the results demonstrated that sample **C** had good chemical stability during photocatalytic H_2 evolution. These three characterizations suggest that the photocatalyst shows long-term stability for photocatalytic reaction.

The catalytic performances of Cu NPs and sample **C** under near-infrared monochromatic light irradiation were also studied, and results are shown in Fig. 4c. Band pass filters were used to block the light above or below specific wavelengths. The H_2 evolution rate decreases to 2.76 and 1.42 mmol g^{-1} h^{-1} when light at a wavelength of 800 nm was used for sample **C** and for Cu NPs, respectively. Similarly, the H_2 evolution rate exhibits a further decrease at the wavelength of 900 nm due to the decreased light energy import. The dependence of the H_2 evolution rates on the different light wavelengths indicates that the photocatalytic reaction over the Cu/rGO catalyst is driven by light and reveals that the H_2 evolution is an electron-driven photocatalytic reaction on Cu NPs [50,51]. Cu NPs absorb the energy of the incident light and yield energetic electrons at the surface of the nanoparticles [52], the light-excited electrons can then participate in the photocatalytic reaction on the surface of Cu NPs and rGO nanosheets for H_2 evolution. Under irradiation by different monochromatic light, sample **C** exhibits a photocatalytic H_2 evolution rate that is superior to Cu NPs alone, indicating that the improvement of photocatalytic activity with
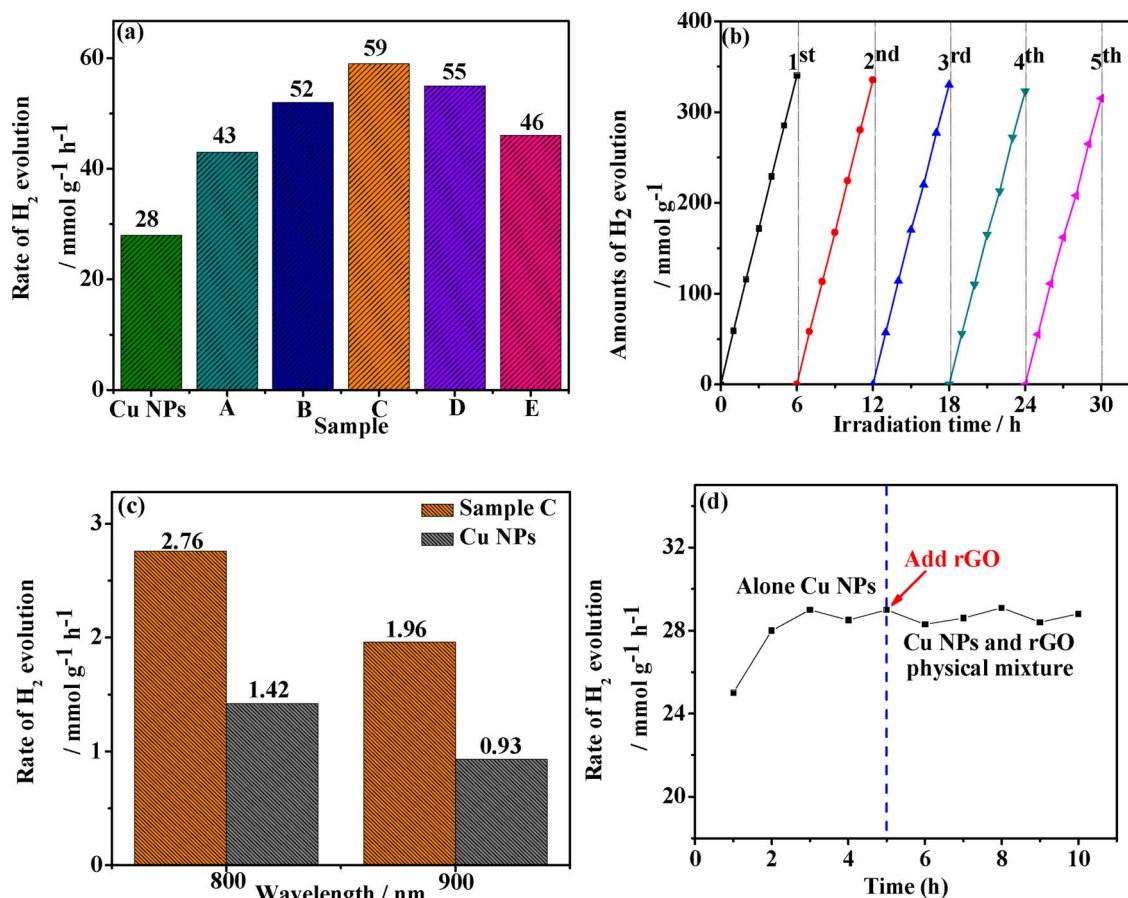
Fig. 4. (a) Hydrogen evolution on Cu NPs, samples **A**, **B**, **C**, **D**, and **E** under solar light irradiation, (b) repeatability of measurements of photocatalytic H_2 evolution for sample **C** (irradiation time = 30 h), (c) photocatalytic H_2 evolution of Cu NPs and sample **C** with near-infrared monochromatic light irradiation and (d) photocatalytic H_2 evolution of physical mixture between Cu NPs and rGO nanosheets.

rGO nanosheets is efficient at different wavelengths. Furthermore, the quantum efficiency (QE) of Cu NPs and sample **C** was obtained with different band-pass filters (λ = 800 and 900 nm), and the results are shown in Table S3.

In addition, the rate of photocatalytic hydrogen evolution was investigated for the physical mixture between Cu NPs and rGO nanosheets and the results are shown in Fig. 4d. At the first hour, the hydrogen evolution rate is relatively low because of the formation of Cu NPs, which could consume a certain time. From the second to the tenth hour, both the physical mixture of Cu NPs-rGO and Cu NPs alone show similar hydrogen evolution rates. No apparent enhancement of hydrogen evolution is achieved with the physical mixture between Cu NPs and rGO nanosheets, suggesting that no efficient contact between rGO nanosheets and Cu NPs was formed. By contrast, the existence of an efficient contact was demonstrated in sample **C**, which can evidently enhance the photocatalytic hydrogen evolution ability (Fig. 4a). In addition, the electrocatalytic HER performances of rGO, Cu nanoparticles and Cu/rGO (sample **C**) were measured by linear sweep voltammetry (LSV), and the results are shown in Fig. S4.

Hydrogen evolution in our system was competitive with the performance of other catalysts reported in the literature. For a better contrast, similar materials were chosen for the hydrogen evolution comparison. Liu et al. reported that Cu NPs were used for hydrogen evolution under sunlight irradiation in a lactic acid aqueous solution, and the highest obtained H_2 evolution rate was 35 mmol g^{-1} h^{-1} [12], which is lower than that of the Cu/rGO nanocomposite. Furthermore, Jiao et al. investigated the photocatalytic H_2 evolution rate of a BiAg alloy and obtained the rate value at the micromolar level [19]. Comparision with other traditional semiconductor photocatalytic systems

such as rGO/Cu$_2$O-Pd [25], rGO/Pt-TiO$_2$ [36], Ag/g-C$_3$N$_4$ [7], Ag/ZrO$_2$ [53], Cu/TiO$_2$ [27], Cu^{2+}-MOF [29], C$_{60}$/Cr$_{2-x}$Fe$_x$O$_3$ [28], Cu-Cu$_2$O/g-C$_3$N$_4$ [13] and Au-Pt/Caln$_2$S$_4$ [54] shows that, their hydrogen evolution rates are also lower than that of the Cu/rGO sample in our study. Importantly, near-infrared photocatalytic ability was obtained in our research, effectively expanding solar light utilization. Most photocatalysts show little response in the near-infrared region and mainly utilize the visible or even the ultraviolet light region. Detailed hydrogen evolution rate data of photocatalysts is listed in Table S4.

3.3. Mechanism

The hydrogen evolution rate depends strongly on the separation of electron-hole pairs, and therefore, transient photocurrents of the samples were acquired during repeated on/off illumination cycles to investigate the charge separation (Fig. 5a). The photocurrent values of the samples exhibit pronounced prompt and reproducible responses upon each illumination and then present a sharp decrease to a steady-state value with the interruption of irradiation. Although similar phenomena were observed for all samples during the on/off illumination cycles, the photocurrent density of sample **C** is the highest and, is about twice as high as that of Cu NPs alone. These results confirm that Cu/rGO separated the photoinduced charge with higher separation efficiency, with rGO nanosheets playing the role of an electron transfer channel that, promotes separation and transfer of electrons from Cu NPs. The generation, separation and migration rates of the photoinduced electrons of samples were also revealed by the quenching of photoluminescence (PL) under 400 nm light excitation (Fig. 5b). Examination of Fig. 5b clearly shows that, the PL intensity decreased from the Cu
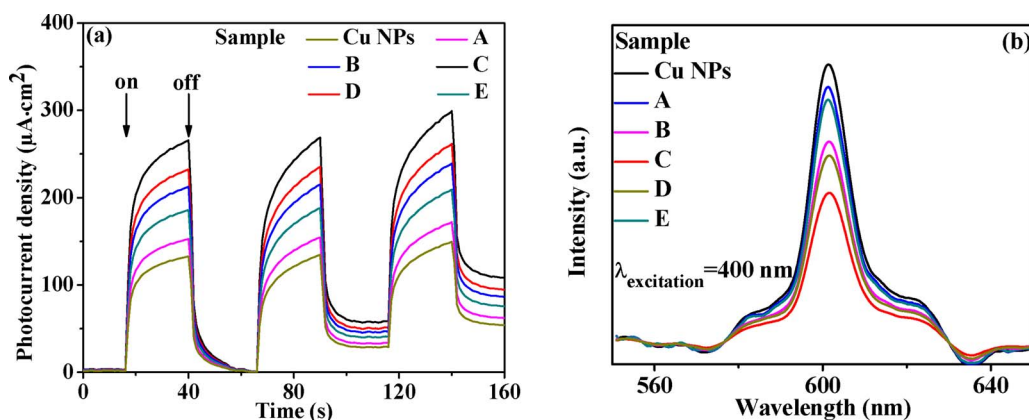
NPs to sample **C**, which is attributed to the efficient charge transfer between the Cu NPs and rGO nanosheets that, prevents the direct electron-holes recombination [55]. Furthermore, atmosphere-controlled steady-state surface photovoltage spectroscopic (SS-SPS) measurements were also performed to probe the charge separation and transfer as shown in Fig. S5. These results suggest that rGO nanosheets played a significant role in promoting efficient separation of photo-induced electron-hole pairs. In particular, the photo-excited electron lifetime of the samples was also determined by time-resolved PL decays, and the results are shown in Table S5. It is obvious that, the longest decay lifetime was obtained for sample **C** as compared to the intrinsic Cu NPs and other Cu/rGO samples, suggesting the action of an accelerated charge transfer mechanism induced by the combination with rGO nanosheets [56].

Based on the above experimental results and analyses, it is crucial and necessary to propose the possible mechanism that, can illustrate the detailed charge transfer circumstances. As shown in Fig. 6, the resonant collective oscillation of electrons in Cu NPs occured with the incident light excitation, followed by decaying into an electron-hole pair through Landau damping [12,14,57]. The accumulated electrons on the Cu NPs will subsequently escape to the neighboring rGO nanosheets for reducing the protons into H_2, whereas the holes on the Cu NPs are captured by lactic acid [58]. Single Cu NPs show a relatively low hydrogen evolution rate because the migration of photoinduced electrons is limited to Cu NPs, resulting in fast charge recombination. The pronounced improvement of the hydrogen evolution rate was obtained when Cu NPs contacted with rGO nanosheets to form the nanohybrid (Fig. 1). The work functions of Cu and rGO are 4.65 and 5.55 eV,

respectively, as is clearly shown in Fig. 6 [59,60]. Hence, electron transfer from Cu to rGO, which is required for H_2 evolution, is thermodynamically favorable. Their unique features make rGO nanosheets display an amazingly high conductivity and electron mobility [16], enabling them to act as an ideal electron sink and/or electron transport bridge to lengthen the lifetime of charge carriers [61], and resulting in the effective separation of electron-hole pairs. Furthermore, rGO nanosheets can also act as a cocatalyst for H_2 evolution, because its reduction potential is more negative than the reduction potential of H^+/H_2 [16].

4. Conclusion

In summary, we have developed a novel type of Cu/rGO nano-photocatalyst using an *in-situ* photoreduction route and, plasmonic Cu NPs deposited, onto the rGO nanosheets surface. This enables, the Cu/rGO to show a two-fold improvement for the photocatalytic H_2 evolution under solar light irradiation compared to the single Cu NPs only. The rGO nanosheets act as the electron mediator for improving the photoinduced carrier separation efficiency, and promote the suppression of electron-hole recombination on the surface of Cu NPs, as well as leave more electrons to participate in H_2 evolution. The Cu/rGO system exhibits an almost full-spectrum-driven photocatalytic activity for H_2 evolution, including the near-infrared region of the spectrum, leading to significant improvement in the light-utilization ability. Furthermore, a remarkable stability of the catalyst was obtained in five consecutive runs, and the photocatalytic hydrogen mechanism was proposed via the photoelectrochemistry measurements. It is anticipated that this work
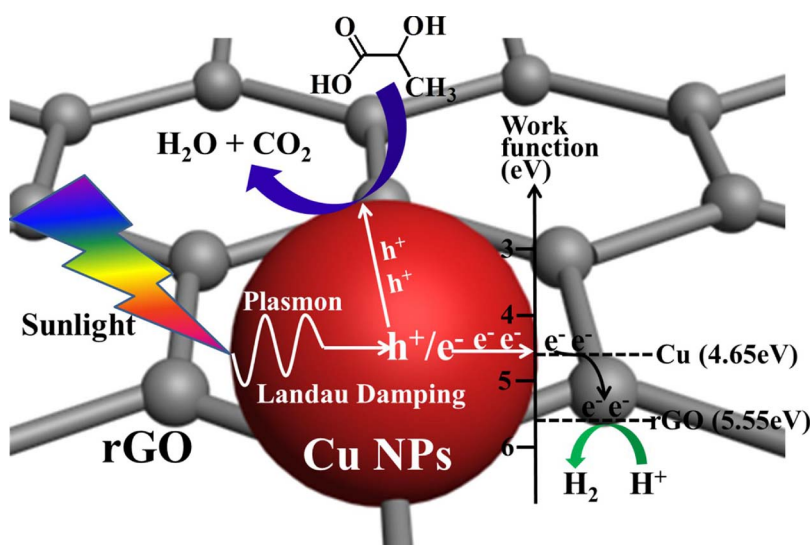
Fig. 6. Schematic of photocatalytic hydrogen evolution over the Cu/rGO system.

will open up new approaches and insights into full-spectrum-driven photocatalytic reactions on the plasmonic metal NPs in the environment and energy field.

Acknowledgements

Appendix A. Supplementary data

Supplementary data associated with this article can be found, in the online version, at https://doi.org/10.1016/j.apcatb.2017.11.076.

References

[1] T. Hisatomi, J. Kubota, K. Domen, Chem. Soc. Rev. 43 (2014) 7520–7535.
[2] X. Zhou, G. Liu, J. Yu, W. Fan, J. Mater. Chem. 22 (2012) 21337–21354.
[3] S. Linic, P. Christopher, D.B. Ingram, Nat. Mater. 10 (2011) 911–921.
[4] C. Clavero, Nat. Photonics 8 (2014) 95–103.
[5] J. Li, S.K. Cushing, F. Meng, T.R. Senty, A.D. Bristow, N. Wu, Nat. Photonics 9 (2015) 601–607.
[6] J. Zeng, T. Song, J. Qin, T. Wang, H. Zeng, RSC Adv. 6 (2016) 54964–54975.
[7] J. Qin, J. Huo, P. Zhang, J. Zeng, T. Wang, H. Zeng, Nanoscale 8 (2016) 2249–2259.
[8] J. Qin, H. Zeng, Appl. Catal. B: Environ. 209 (2017) 161–173.
[9] A. Marimuthu, J.W. Zhang, S. Linic, Science 339 (2013) 1590–1593.
[10] S. Sarina, H.Y. Zhu, E. Jaatinen, Q. Xiao, H.W. Liu, J.F. Jia, C. Chen, J. Zhao, J. Am. Chem. Soc. 135 (2013) 5793–5801.
[11] Y. Zhang, S.J. Park, J. Catal. 355 (2017) 1–10.
[12] H. Liu, T. Wang, H. Zeng, Part. Part. Syst. Char. 32 (2015) 869–873.
[13] P. Zhang, T. Wang, H. Zeng, Appl. Surf. Sci. 391 (2017) 404–414.
[14] P. Zhang, T. Song, T. Wang, H. Zeng, Appl. Catal. B: Environ. 206 (2017) 328–335.
[15] Y. Zhang, M. Park, H.Y. Kim, B. Ding, S.J. Park, Appl. Surf. Sci. 384 (2016) 192–199.
[16] G. Xie, K. Zhang, B. Guo, Q. Liu, L. Fang, J. Gong, Adv. Mater. 25 (2013) 3820–3839.
[17] P. Wang, S. Zhan, Y. Xia, S. Ma, Q. Zhou, Y. Li, Appl. Catal. B: Environ. 207 (2017) 335–346.
[18] X. Zhang, Z. Wang, N. Meng, D.T. McCarthy, A. Deletic, J. Pan, X. Zhang, Appl. Catal. B: Environ. 202 (2017) 33–41.
[19] Z. Jiao, Y. Zhang, S. Quyang, H. Yu, G. Lu, J. Ye, Y. Bi, Appl. Mater. Interfaces 6 (2014) 19488–19493.
[20] Y. Ma, Y. Jia, L. Wang, M. Yang, Y. Bi, Y. Qi, Chem. Eur. J. 22 (2016) 5844–5848.
[21] Z. Jiao, M. Shang, J. Liu, G. Lu, X. Wang, Y. Bi, Nano Energy 31 (2017) 96–104.
[22] T. Wang, B. Jin, Z. Jiao, G. Lu, J. Ye, Y. Bi, J. Mater. Chem. A 2 (2014) 15553–15559.
[23] X. Wang, L. Zhi, K. Mullen, Nano Lett. 8 (2007) 323–328.
[24] G. Zerjav, M.S. Arshad, P. Djinovic, I. Junkar, J. Kovac, J. Zavasnik, A. Pintar, Nanoscale 9 (2017) 4578–4592.
[25] S. Bai, J. Ge, J. Jiang, Q. Zhang, Y. Xiong, Adv. Mater. 26 (2014) 5689–5695.
[26] Y. Zhang, S.J. Park, Carbon 122 (2017) 287–297.
[27] P. Zhang, T. Song, T. Wang, H. Zeng, RSC Adv. 7 (2017) 17873–17881.
[28] T. Song, J. Huo, T. Liao, J. Zeng, J. Qin, H. Zeng, Chem. Eng. J. 287 (2016) 359–366.
[29] T. Song, L. Zhang, P. Zhang, J. Zeng, T. Wang, A. Ali, H. Zeng, J. Mater. Chem. A 5 (2017) 6013–6018.
[30] W.S. Hummers Jr., R.E. Offeman, J. Am. Chem. Soc. 80 (1958) 1339.
[31] W. Wang, Y. Li, Z. Kang, F. Wang, J.C. Yu, Appl. Catal. B: Environ. 182 (2016) 184–192.
[32] J.C. Meyer, C. Kisielowski, R. Erni, M.D. Rossell, M.F. Crommie, A. Zettl, Nano Lett. 8 (2008) 3582–3586.
[33] G.P. Sing, K.M. Shrestha, A. Nepal, K.J. Klabunde, C.M. Sorensen, Nanotechnology 26 (2014) 265701–265712.
[34] S. Zhang, Y. Ma, H. Zhang, X. Zhou, X. Chen, Y. Qu, Angew. Chem. Int. Ed. 56 (2017) 1–6.
[35] J. Yang, X. Shen, Z. Ji, H. Zhou, G. Zhu, K. Chen, Appl. Surf. Sci. 316 (2014) 575–581.
[36] Y. Chen, F. Sun, Z. Huang, H. Chen, Z. Zhuang, Z. Pan, J. Long, F. Gu, Appl. Catal. B: Environ. 215 (2017) 8–17.
[37] G. Li, T. Wang, Y. Zhu, S. Zhang, C. Mao, J. Wu, B. Jin, Y. Tian, Appl. Surf. Sci. 257 (2011) 6568–6572.
[38] Q. Xiang, J. Yu, M. Jaroniec, J. Phys. Chem. C 115 (2011) 7355–7363.
[39] P. Wang, J. Wang, X. Wang, H. Yu, J. Yu, M. Lei, Y. Wang, Appl. Catal. B: Environ. 132–133 (2013) 452–459.
[40] H. Li, Z. Xia, J. Chen, L. Lei, J. Xing, Appl. Catal. B: Environ. 168–169 (2015) 105–113.
[41] Y. Sang, Z. Zhao, J. Tian, P. Hao, H. Jiang, H. Liu, J.P. Claverie, Small 10 (2014) 3775–3782.
[42] X. Pan, Y. Zhao, S. Liu, C.L. Korzeniewski, S. Wang, Z. Fan, ACS Appl. Mater. Interfaces 4 (2012) 3944–3950.
[43] T.M.G. Mohiuddin, A. Lombardo, R.R. Nair, A. Bonetti, G. Savini, R. Jalil, Phys. Rev. B 79 (2009) 1–9.
[44] E.Z. Liu, L.M. Kang, Y.H. Yang, T. Sun, X.Y. Hu, C.J. Zhu, Nanotechnology 25 (2014) 165401.
[45] Y. Hou, Z. Wen, S. Cui, X. Guo, J. Chen, Adv. Mater. 25 (2013) 6291–6297.
[46] H. He, C. Gao, Chem. Mater. 22 (2010) 5054–5064.
[47] D.P. Kumar, S. Hong, D.A. Reddy, T.K. Kim, Appl. Catal. B: Environ. 212 (2017) 7–14.
[48] J.G. Yu, H.G. Yu, B. Cheng, X.J. Zhao, J.C. Yu, J. Phys. Chem. B 107 (2003) 13871–13879.
[49] X. Zhang, H. Li, X. Cui, Y. Lin, J. Mater. Chem. 20 (2010) 2801–2806.
[50] D.G. Busch, W. Ho, Phys. Rev. Lett. 77 (1996) 1338–1341.
[51] P. Christopher, H.L. Xin, A. Marimuthu, S. Linic, Nat. Mater. 11 (2012) 1044–1050.
[52] J. Bosbach, C. Hendrich, F. Stietz, T. Vartanyan, F. Träger, Phys. Rev. Lett. 89 (2002) 257404.
[53] J. Zhang, L. Li, S. Wang, T. Huang, Y. Hao, Y. Qi, RSC Adv. 6 (2016) 13991–14001.
[54] J. Ding, X. Li, C. Gao, X. Tian, J. Mater. Chem. A 4 (2016) 12630–12637.
[55] H. Li, S. Gan, H. Wang, D. Han, L. Niu, Adv. Mater. 27 (2015) 6906–6913.
[56] J. Hou, H. Chen, O. Takeda, H. Zhu, Angew. Chem. Int. Ed. 54 (2015) 8480–8484.
[57] H. Petek, S. Ogawa, Prog. Surf. Sci. 56 (1997) 239–310.
[58] J. Chen, X. Wu, L. Yin, B. Li, X. Hong, Z. Fan, Angew. Chem. Int. Ed. 54 (2015) 1210–1214.
[59] Z. Lin, J. Li, L. Li, L. Yu, W. Li, G. Yang, J. Mater. Chem. A 5 (2017) 773–781.
[60] P.V. Kumar, M. Bernardi, J.C. Grossman, ACS Nano 7 (2013) 1638–1645.
[61] P. Chen, T. Xiao, H. Li, J. Yang, Z. Wang, H. Yao, S. Yu, ACS Nano 6 (2012) 712–719.